Ultrasonics Sonochemistry 83 (2022) 105921

Contents lists available at ScienceDirect

Ultrasonics Sonochemistry

journal homepage: www.elsevier.com/locate/ultson

Ultrasound-aided synthesis of gold-loaded boron-doped graphene quantum dots interface towards simultaneous electrochemical determination of guanine and adenine biomolecules

Reshma Kaimal [a], Patel Nishant Mansukhlal [a], Belqasem Aljafari [b], Sambandam Anandan [a,*], Muthupandian Ashokkumar [c]

[a] Nanomaterials & Solar Energy Conversion Lab, Department of Chemistry, National Institute of Technology, Tiruchirappalli 620015, India
[b] Department of Electrical Engineering, College of Engineering, Najran University, Najran 11001, Saudi Arabia
[c] School of Chemistry, University of Melbourne, Vic 3010, Australia

ARTICLE INFO

Keywords:
Cyclic voltammetry
Boron graphene quantum dots
Gold nanoparticles
Guanine
Adenine

ABSTRACT

To acquire substantial electrochemical signals of guanine-GUA and adenine-ADE present in deoxyribonucleic acid-DNA, it is critical to investigate innovative electrode materials and their interfaces. In this study, gold-loaded boron-doped graphene quantum dots (Au@B-GQDs) interface was prepared via ultrasound-aided reduction method for monitoring GUA and ADE electrochemically. Transmission electron microscopy-TEM, Ultraviolet–Visible spectroscopy-UV–Vis, Raman spectroscopy, X-ray photoelectron spectroscopy-XPS, cyclic voltammetry-CV, and differential pulse voltammetry-DPV were used to examine the microstructure of the fabricated interface and demonstrate its electrochemical characteristics. The sensor was constructed by depositing the as-prepared Au@B-GQDs as a thin layer on a glassy carbon-GC electrode by the drop-casting method and carried out the electrochemical studies. The resulting sensor exhibited a good response with a wide linear range (GUA = 0.5–20 μM, ADE = 0.1–20 μM), a low detection limit-LOD (GUA = 1.71 μM, ADE = 1.84 μM), excellent sensitivity (GUA = 0.0820 $\mu A \mu M^{-1}$, ADE = 0.1561 $\mu A \mu M^{-1}$) and selectivity with common interferents results from biological matrixes. Furthermore, it seems to have prominent selectivity, reproducibility, repeatability, and long-lasting stability. The results demonstrate that the fabricated Au@B-GQDs/GC electrode is a simple and effective sensing platform for detecting GUA and ADE in neutral media at low potential as it exhibited prominent synergistic impact and outstanding electrocatalytic activity corresponding to individual AuNPs and B-GQDs modified electrodes.

1. Introduction

Deoxyribonucleic acid-DNA is a significant bio functional macromolecule involved in the encoding of genetic data as well as protein creation. All living organisms have such genetic material in their cells. DNA is composed of four different varieties of deoxyribonucleotide monomers that form a block copolymer [1,2]. In biological sciences, nucleobase analysis is crucial, particularly in the diagnosis of infectious illnesses and the research of genetic alterations. They can impact numerous genetic illnesses such as metabolic disorders, vision and hearing loss, blood diseases, and neurodegenerative diseases by storing and transmitting biological information. Purine bases (Guanine-GUA and Adenine-ADE) are constituted in DNA and serve a role in cellular energy transmission and signaling through enzymatic oxidation processes [3]. According to the Watson-Crick DNA base pairing mechanism, [Adenine] = [Thymine] and [Guanine] = [Cytosine], i.e., the mole percentage of adenine equals thymine, and the mole percentage of guanine equals cytosine [4]. Failure to identify mutations can result in

Abbreviations: ADE, Adenine; Au@B-GQDs, Gold loaded boron doped graphene quantum dots; AuNPs, Gold nanoparticles; B-GQDs, Boron doped graphene quantum dots; CV, Cyclic Voltammetry; DI, Distilled water; DNA, Deoxyribonucleic Acid; DPV, Differential Pulse Voltammetry; EDX, Energy dispersive X-Ray; Fcc, face-centered cubic; GCE, Glassy carbon electrode; GUA, Guanine; GQDs, Graphene quantum dots; HIV, Human immunodeficiency virus; HRTEM, High-resolution transmission electron microscopy; LOD, Limit of detection; PBS, Phosphate buffer solution; pH, Potential of hydrogen; RSD, Relative standard deviation; SAED, Selected area electron diffraction; UV–Vis, Ultraviolet–Visible; XPS, X-ray photoelectron spectroscopy.

* Corresponding author.
E-mail address: sanand@nitt.edu (S. Anandan).

https://doi.org/10.1016/j.ultsonch.2022.105921
Received 19 December 2021; Received in revised form 10 January 2022; Accepted 14 January 2022
Available online 19 January 2022

cell death or apoptosis, disruption of gene expression, and cancer, all of which can harm the organism's health. Heart and muscle illness can be caused by a simple mutation in mitochondrial DNA. As a result, aberrant alterations in DNA bases in organisms cause a weakness in the immune system and may signal the existence of an array of disorders, such as cancer, HIV infection, epilepsy, and Alzheimer's disease [5,6]. The identification of DNA bases is crucial for clinical diagnosis and research into the mechanisms occurring behind each genetic information [7,8]. Detecting DNA alterations is crucial, as is determining the best approaches to prevent or treat illness [9,10]. Different experimental techniques (Microchip capillary electrophoresis, flow injection chemiluminescence, ion-pairing liquid chromatography, laser-induced fluorescence detection, and micellar electrokinetic chromatography) have all been developed to identify DNA bases[11–17]. Although these approaches have certain advantages, they frequently require expensive apparatus, difficult processes, or time-consuming sample pre-treatments [18]. Because of its benefits of speed, comfort, cheap expense, and ease of quantization for small-volume samples, electrochemical methods seem favorable for the study of bases present in DNA [19].

Complex efforts have lately been taken to improving the analytic performance. Because of the superior conductivity, biocompatibility, and larger surface area, carbon-based nanoarchitecture materials have found widespread application in sensing and energy storage devices. Graphene quantum dots-GQDs are a type of nanostructured material that have recently gained a great deal of interest. Through various chemical modifications, graphene quantum dots (GQDs), which are zero-dimensional densely packed honeycomb graphene nanosheets with a size of less than 100 nm, are used as an effective material in electrochemical applications. When compared to 2D zero-bandgap graphene sheets, GQDs have stimulated significant and growing research interest due to its exceptional features connected with quantum confinement and edge effects [20,21]. Biocompatibility, chemical inertness, toxicity, and conductivity are all advantages of GQDs. They are promising candidates for biosensing, cell imaging, and as a class of solar cells and bioimaging probes [22,23]. The disadvantages of GQDs for electrochemical applications are poor electrical conductivity and their small size to form the network for electron transport. In this regard, heteroatom doping can enhance the structural, optical, physical, and chemical properties of GQDs. The incorporation of heteroatoms (such as B, N, and S) into nanocarbon materials is frequently used to enhance their fundamental electrical and chemical properties by altering their electronic structure. Concerning materials without doping, B-doped materials have shown a significant increase in electrical characteristics compared to materials with other dopants [24]. Because carbon-C and boron-B atoms have similar sizes, B may be readily doped by swapping a C atom in the GQDs lattice structure. B has an electron shortage, i.e., because of their lower electronegativity than C atoms, B atoms integrated with C atoms have a positive charge; therefore, its doping is expected to improve pure graphene's p-type conducting behavior, resulting in nano electrical device applications [25] towards sensors [26], energy generation [27], storage [28], biomedicine [29], and photocatalysis [30–35]. Thereby, the synthesis of boron-doped graphene quantum dots could be an effective strategy for increasing the electron transfer ability of graphene quantum dots which makes it an excellent choice for highly efficient electron transfer in electrochemical applications. The composites of the NPs and the hetero atom doped quantum dots can retain the qualities of each component while also providing synergistic benefits through cooperative contacts, resulting in essential aspects including increased surface area, greater electrocatalytic activity, better biocompatibility, and better electron transfer. Consequently, this type of carbon material was adopted as the conducting electrode for the fabricated electrochemical biosensor.

Furthermore, the introduction of Au onto the electrochemical interfaces has infused new vigor into electrochemistry. AuNPs have received increased interest from electroanalytical chemists due to their outstanding analytical compatibility, high surface-to-volume ratio, and superior conducting capabilities [36]. AuNPs' ability to bind to a variety of biomolecules, as well as their strong electron-e^{-} capture properties, made them a highly efficient metal for adsorbing biomolecules. AuNPs modified electrode surfaces have recently been reported in vast numbers, resulting in functional electrochemical sensing interfaces [37,38]. Once the nanometer scale Au particles covered the surface of the supporting electrode comes into contact with the biological analyte, rapid e- capture occurs, while carbon materials like quantum dots, as the supporting electrode, quickly transfer these electrons, thereby enhancing the electrode's catalytic activity and boosting the intensity and speed of ion-current conversion to electron current [39]. With the improvement of nanotechnology and nanoscience, metal nanoparticles have a significant role in many fields like nanosensors, catalysis, surface-enhanced Raman scattering, biological labeling, microelectronics and biomedicine due to their distinctive catalytic, thermal, electrical and optical properties [40]. Metal nanoparticles have large potential outcomes in biosensor performance because of their considerable surface-to-volume ratio, surface reaction activity, excellent electrical conductivity, great biocompatibility, and efficient synergist limit. Thus, nanoscale Au particles had excellent catalytic activities for the oxidation of purine bases in DNA.

This study presents, to our knowledge, the first comparative evaluation of the electrocatalytic characteristics of electrodes modified using composite materials based on boron-doped graphene quantum dots (B-GQDs) and gold nanoparticles (AuNPs). A laterally developed layer of B-GQDs interacts with AuNPs to form a highly selective and sensitive - biosensor. They have been examined in the presence of GUA and ADE using several electrochemical methods (cyclic voltammetry-CV, differential pulse voltammetry-DPV) and may be detected concurrently on the as-prepared composite with good sensitivity across a wide linear range. Eventually, the behavior of the newly fabricated electrode is assessed in the existence of biological interferents such as different ions (glucose, uric acid, ascorbic acid, and urea). Subsequently, the repeatability, reproducibility, linear range, stability, selectivity, the limit of detection, and sensitivity are established. The findings of these electrochemical studies were reinforced by those acquired using other latest methods, like HRTEM, UV–Vis, Raman spectroscopy, and XPS, which provided us with information on the composite materials' morphological and structural features.

2. Experimental procedures

2.1. Synthesis methods

The sonochemical approach was employed to synthesize Au@B-GQDs in this work, which was a simple and environmentally benign process. The preparation procedures employed for Au@B-GQDs nanocomposite are schematically illustrated in Scheme 1. Au^{3+} was converted to AuNPs in the first stage using a conventional stirring process. Secondly, B-GQDs are prepared by hydrothermal approach by combining glucose and boric acid at 160 °C for 3 hrs. Finally, AuNPs are then ultrasonically loaded onto the hydrothermally produced B-GQDs. The section following has more extensive explanations.

2.1.1. Preparation of gold nanoparticles (AuNPs)

In a 20 mL beaker, gold nanoparticles were generated by diluting CTAB (0.1 M) with ultrapure double distilled water (8 mL), then added KI (0.01 M, 75 μL), $HAuCl_4$ (25.4 mM, 80 μL), and NaOH (0.1 M, 20.3 μL) in the same order results in a light yellowish colored solution. With moderate shaking, ascorbic acid (0.064 M, 80 μL) was introduced into the solution, results fading of yellowish color to a colorless state. Finally, 10 μL of NaOH (0.1 M) was introduced into the beaker with vigorously shaking for 2 s. Scheme 2 shows the mechanistic details: Cetyltrimethylammonium bromide (CTAB) was explored as the surfactant as well as protecting nanoparticles from aggregation, and iodide ions were used as the shape-directing agent. The halide ions in gold nanoparticle

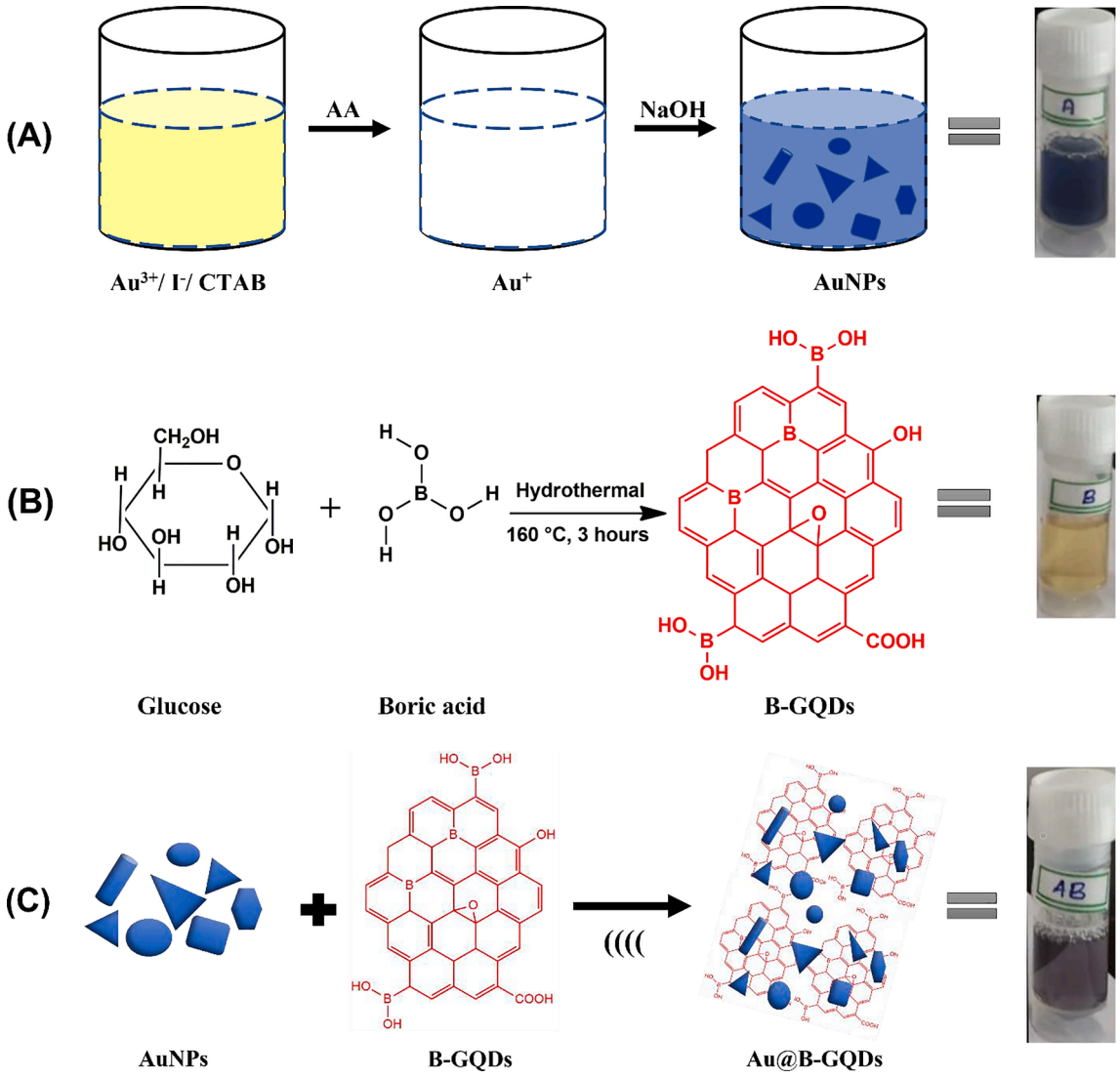

Scheme 1. Schematic illustration for the preparation of AuNPs (a), B-GQDs (b), and Au@B-GQDs (c) composite materials.

synthesis utilizing cetyltrimethylammonium halide (CTA)-X (X = halide), where CTA-Au-X complexes played an essential role in guiding nanoparticle shape progression [41]. Due to electrostatic forces, the CTAB bilayer is present on all surfaces without iodide ions, resulting in a lack of preferential development and an isotropic nanoparticle. Because of its dominant specific adsorption on an iodide adlayer (CTA^+-I^-) compared to other halide ions, a stable CTAB bilayer forms preferentially in the presence of iodide ions and passively regulates the supply of additional chemicals for the gold surface [42,43]. Sodium hydroxide was used to adjust the pH of the growth solution. Upon the addition of ascorbic acid (mild reducing agent), Au^{3+} was quickly reduced to Au^+, as evidenced by the colour change of the solution from light yellowish to colourless. Finally, a certain amount of NaOH was added into the solution quickly to start the Au^+ reduction process. With the addition of NaOH, the previously colourless solution turns light reddish, indicating that Au^+ has been reduced to AuNPs. The colorless solution changed to reddish-purple and then to blue over time. The growth process can be achieved in 10 min [44]. The resultant AuNPs solution was allowed to cool naturally before being kept at 4 °C until needed.

2.1.2. Preparation of boron doped graphene quantum dots (B-GQDs)

4 g of glucose was dissolved in 40 mL of deionized water (DI), then 16 mg of boric acid was added (0.4 wt%). The mixture was transferred to a 100 mL Teflon-lined stainless-steel autoclave and hydrothermally treated for 3 h at 160 °C after 3 h of stirring at ambient temperature. A light-orange tinted solution was formed after cooling to ambient temperature [45].

2.1.3. Preparation of gold loaded boron doped graphene quantum dots (Au@B-GQDs)

Finally, the Au@B-GQDs were made utilizing an environmentally safe ultrasonication process. For ultrasonic irradiation, a sonication device (Kaijo 30110 (QR – 003) model, frequency, 38 kHz; power, 50 W) was utilized. 1:1 (v/v) ratio (1 mL of AuNPs along with 1 mL of B-GQDs) was taken in a test tube and was sonicated at 50 W for 1 h. In the end, a reddish-purple coloured solution was obtained. The generated sample was directly employed for characterization tests and electrochemical applications after the synthesis method. There was no separation or drying procedure used in this case. Sonochemistry uses cavitation as it is the most important of the effects because the most significant chemical implications occur from the creation and collapse of microbubbles, resulting in extraordinarily high pressures and temperatures. Chemical synthesis aided by ultrasonication is widely recognized for saving reaction time and chemical consumption. Furthermore, ultrasonication has been shown to aid in the production of nanoparticles of various morphologies.

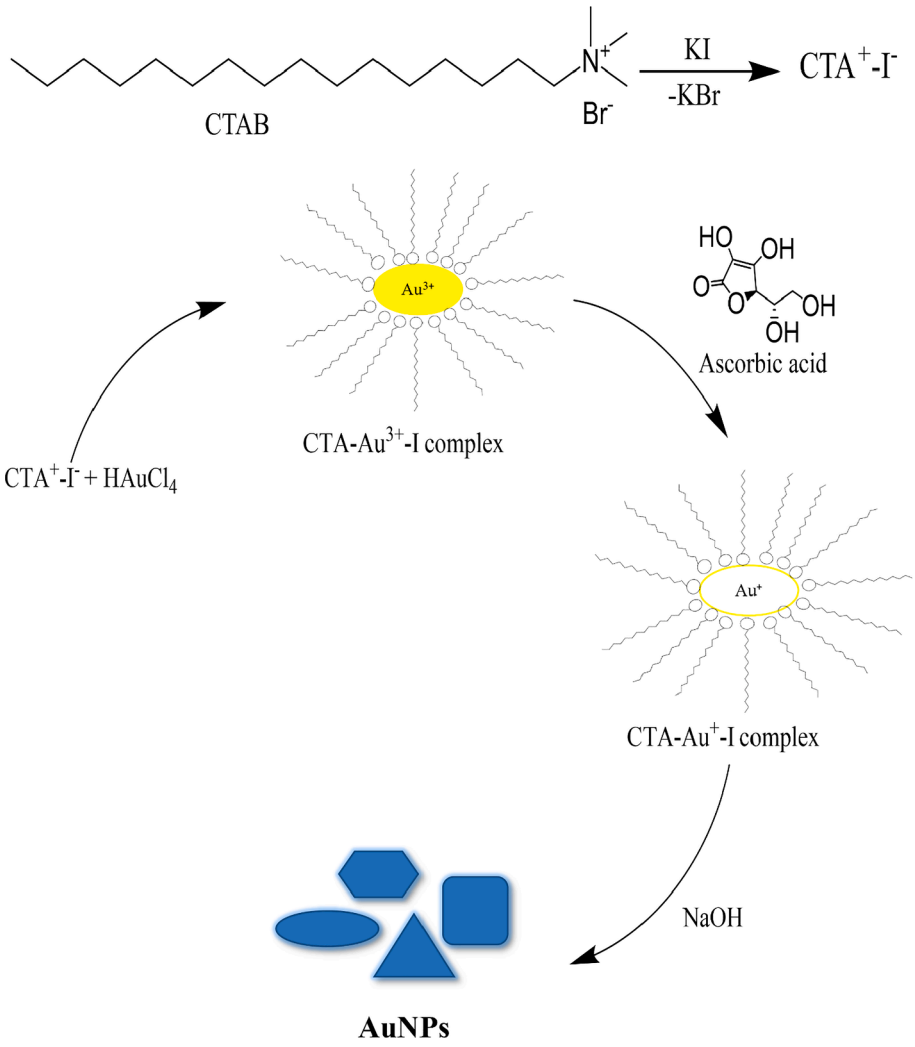

Scheme 2. Schematic illustration of synthesizing gold nanoparticles.

2.2. Real sample preparation

To determine GUA and ADE, a calf thymus DNA sample was hydrolyzed. In a sealed 10 mL glass tube, 1 mL of 1 M HCl was used to digest 3 mg of calf thymus DNA. 1 mL of 1 M NaOH was used to alter the pH of the solution after it had been heated in a boiling water bath for 60 min. The required amount of this solution was added to a 10 mL buffer solution in the electrochemical cell (pH 7) [46].

The recovery percentage was determined by analyzing spiked sample solutions according to the suggested analytical procedure:

$$Recovery(\%) = \frac{(S_{Spiked} - R_{Real})}{S_{Spiked}} \times 100 \quad (1)$$

where S_{Spiked} represents the calculated analyte concentration in the spiked sample (μg/mL) and R_{Real} stands for the concentration of the analyte in the real sample solution (μg/mL).

3. Results and discussion

3.1. Characterization of materials as-prepared

The morphology and microstructure of synthesized B-GQDs, AuNPs, and Au@B-GQDs were examined chiefly using transmission electron microscopy (TEM), energy dispersive X-Ray (EDX) analyses, selected area electron diffraction (SAED). In supporting information, the results for AuNPs and B-GQDs are provided (Fig. S1 & S2). The HRTEM images of AuNPs which exhibited a mixture of triangles, hexagons, cubes, and spheres having an average diameter of 40 ± 6 nm (Fig. S1(a-b)). Fig. S1c shows an HRTEM image of single Au crystal (perfect atomic arrangement). The AuNPs are crystalline in nature, as evidenced by the distinct lattices. The diffraction pattern derived from AuNPs is depicted in Fig. S1d, with rings corresponding to the (111), (200), (311), and (222) reflections of gold's face-centered cubic (fcc) structure [47]. HRTEM scans of B-GQDs notify modest particle sizes ranging from 2 to 6 nm that are densely and consistently scattered (See Fig. S2(a-b)). The HRTEM image of B-GQDs (Fig. S2c) indicates that they are extremely crystalline, with a lattice spacing of 0.240 nm that corresponds to the (1 1 2 0) graphene lattice constant, which is greater than that of undoped GQDs (0.21 nm) [48,49]. The SAED pattern showed diffraction rings caused by randomly oriented nanocrystals, validating the crystallinity of the produced B-GQDs (Fig. S2d).

Fig. 1 shows the results obtained after incorporation of AuNPs on B-GQDs. It is found that after ultrasonic treatment, the Au nanoparticles are strongly bound to the B-GQDs and have a size in the range 45 ± 15 nm, i.e., gold nanoparticles with different morphologies are dispersed on the B-GQDs film surface uniformly (Fig. 1(c)). The B-GQDs layer is grown laterally and over which Au nanoparticles are anchored to create a biosensor that is highly selective and sensitive. (Fig. 1b). In Fig. 1d, the SAED patterns showed that the composite is polycrystalline as same as AuNPs. The bright-field TEM image of as-prepared Au@B-GQDs and the corresponding elemental color mapping of B, C, and Au are provided in

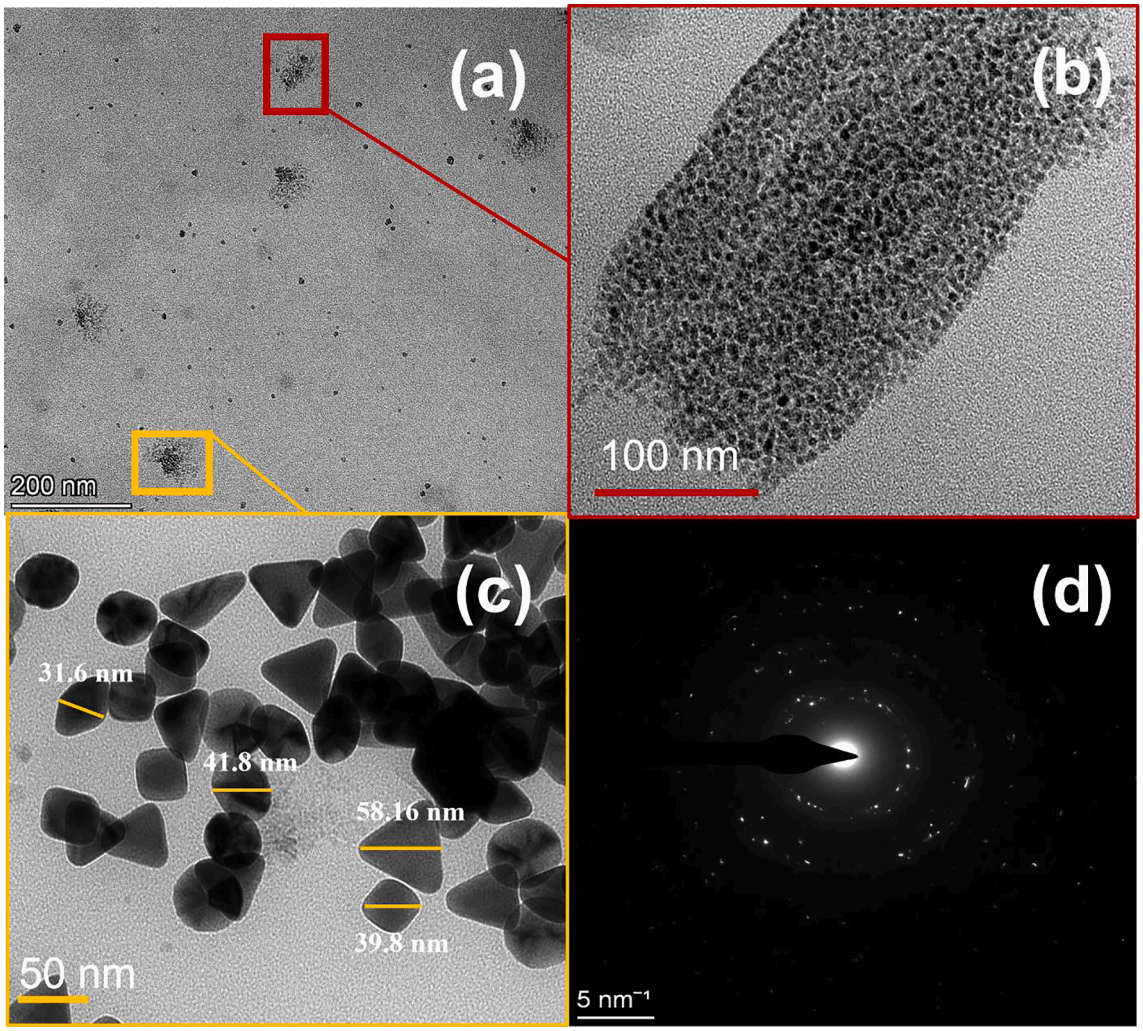

Fig. 1. TEM images of Au@B-GQDs (a-c) and SAED pattern for Au@B-GQDs (d) at various scale magnifications.

Fig. 2. The EDX spectrum of Au@B-GQDs nanocomposite confirms the presence of constituents such as B, C, and Au. This certifies the successful preparation of the target material (Au@B-GQDs).

Fig. 3 studies reveal the optical properties of the as-prepared AuNPs, B-GQDs, and Au@B-GQDs nanocomposite. In Fig. 3a, AuNPs show a UV–Vis absorption spectrum at 550 nm and small peaks between 800 and 1200 nm indicating that the gold nanoparticles have been formed with different morphologies which include the spherical shape. Fig. 3b shows the UV − Vis absorption spectrum of B-GQDs which shows a peak at 230 nm designated to the π to π* transition of aromatic sp^2 domain [50]. Peak around 280 nm is assigned as n to π* transitions of non-bonding electrons of oxygen atoms involved in C = O and/or C-O bonds. In the case of Au@B-GQDs, characteristic peaks of both AuNPs and B-GQDs are noticed. The UV–Visible spectrum confirms the formation of Au@B-GQDs through a sonochemical approach. These findings are consistent with those obtained by TEM analysis, establishing that nanoparticles were formed using the sonochemical synthesis approach.

Fig. 4 shows studies regarding Raman analysis of B-GQDs and Au@B-GQDs. Fig. 4a exhibit two remarkable peaks for B-GQDs at 1390 cm^{-1} and 1542 cm^{-1} which corresponds to the distinct D and G band, respectively. The degree of graphitization may be explained using the G band, which is correlated with the E_{2g} vibration mode of sp^2 carbon domains, while the D band is linked to structural imperfections and partially disordered sp^2 domain structures [50–52]. Fig. 4b exhibit two remarkable peaks for Au@B-GQDs at 1383 cm^{-1} and 1558 cm^{-1}. The upshift of the G band in Au@B-GQDs, when compared to B-GQDs, suggests the fact that Au@B-GQDs is doped with p-type of dopant. Previous research has established that the G band in Raman spectra is a sign of p-type doping owing to upshift of band and that this is the case here due to the implementation of Boron and gold over graphene quantum dots [53]. The I_D/I_G ratio in the Raman spectra is widely used to assess graphene materials' structural disorder. It was found out that I_D/I_G ratio for B-GQDs and Au@B-GQDs are 0.9067 and 0.8876 respectively. The reduced I_D/I_G ratio suggests that the graphitic framework has been effectively restored structurally. However, the Au@B-GQDs have a wider D band than B-GQDs, indicating that the immobilization of Au atoms into the conjugated carbon backbone has resulted in relatively disordered structures.

XPS tests were carried out to gain a better understanding of gold and boron doping in graphene quantum dots, as well as the chemical composition of Au@B-GQDs. (Fig. 5). Fig. 5a depicts survey spectra of Au@B-GQDs, which include O1s, C1s, B1s, and Au4f peaks with no additional impurities found. Fig. 5b demonstrated two peaks of Au4f at 83.4 eV and 87.1 eV that are allocated to $Au4f_{7/2}$ and $Au4f_{5/2}$, respectively [54]. In Fig. 5c, the B1s spectrum is represented and is deconvoluted into two peaks as B_4C (denoted as B-C*) (187.5 eV) and B-C (189.03 eV) were observed, which confirms the boron doping into the carbon matrix [55]. The peaks in the C1s spectrum indicate the appearance of C–C (284.5 eV), C-O (285.9 eV), and C = O (287.3 eV).

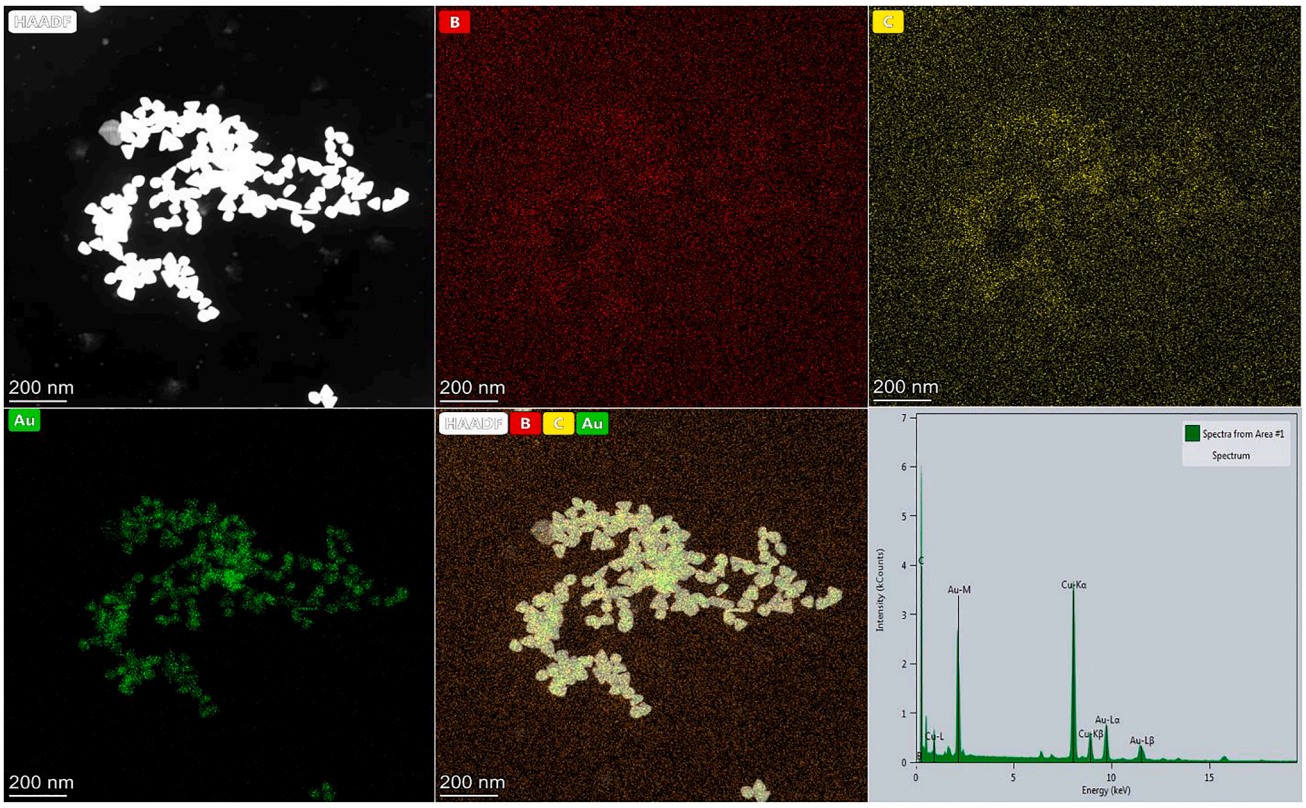

Fig. 2. Bright-field TEM image of Au@B-GQDs and the resulting elemental color mapping of B, C, and Au. The final image is the EDX spectra of Au@B-GQDs. The emission peaks associated with Cu appeared from the supporting microscopic grid.

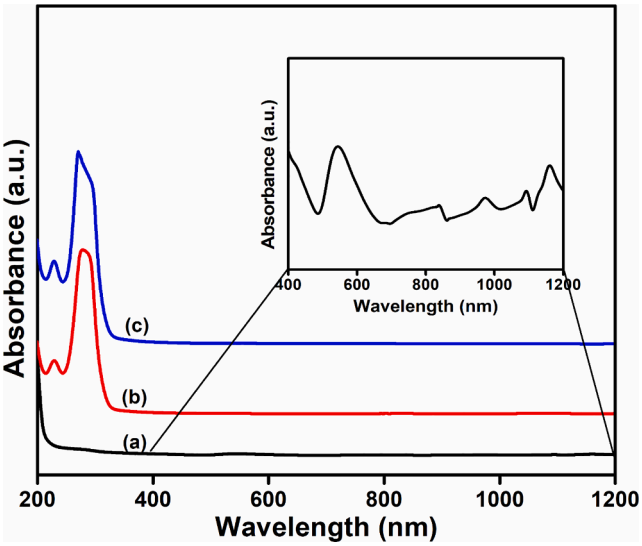

Fig. 3. UV–Vis spectra of (a) AuNPs, (b) B-GQDs, and (c) Au@B-GQDs. Inset: Zoomed image of AuNPs.

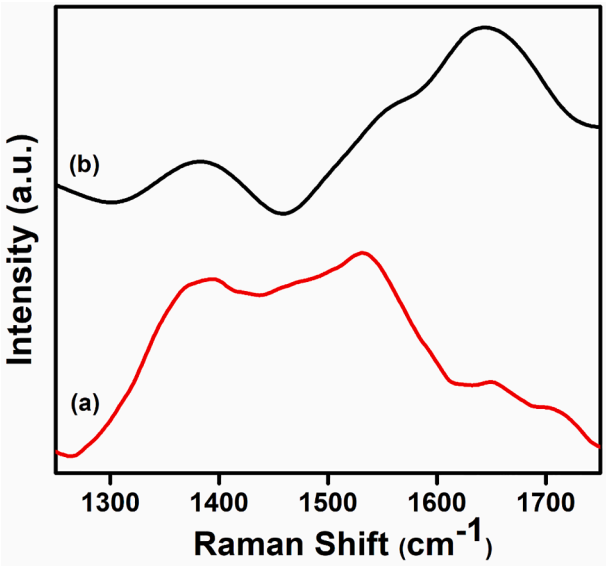

Fig. 4. Raman spectra of B-GQDs (a) and Au@B-GQDs (b).

3.2. Electrocatalytic oxidation of GUA and ADE

Fig. 6 illustrates electrochemical activities using cyclic voltammogram responses of (a) Bare/GCE, (b) AuNPs/GCE, (c) B-GQDs/GCE, and (d) Au@B-GQDs/GCE modified electrodes using $[Fe(CN)_6]^{3-/4-}$ as a redox couple solution (5 mM $K_3[Fe(CN)_6]$ in 0.1 M KCl). The format of the redox peaks is relatively broad at the bare GCE (Fig. 6a), and the peak potential separation (ΔE_p) is relatively high with low background current. Upon the modification of the GC electrode surface with AuNPs and B-GQDs, redox peaks were not distinguishable and the peak currents of the system increased regarding AuNPs and B-GQDs/GC electrode while the peak separation notably increased as well, i.e., having a large peak to peak separation (Fig. 6b and 6c). Au@B-GQDs modified GC electrode (Fig. 6d) also shows a reduced peak-to-peak separation, and the large background currents indicate that the electron kinetic rate is improved, hence an excellent electrochemical catalytic behavior was attained. Such findings show that the increased surface area supplied by the Au@B-GQDs modified GC electrode significantly improves electron

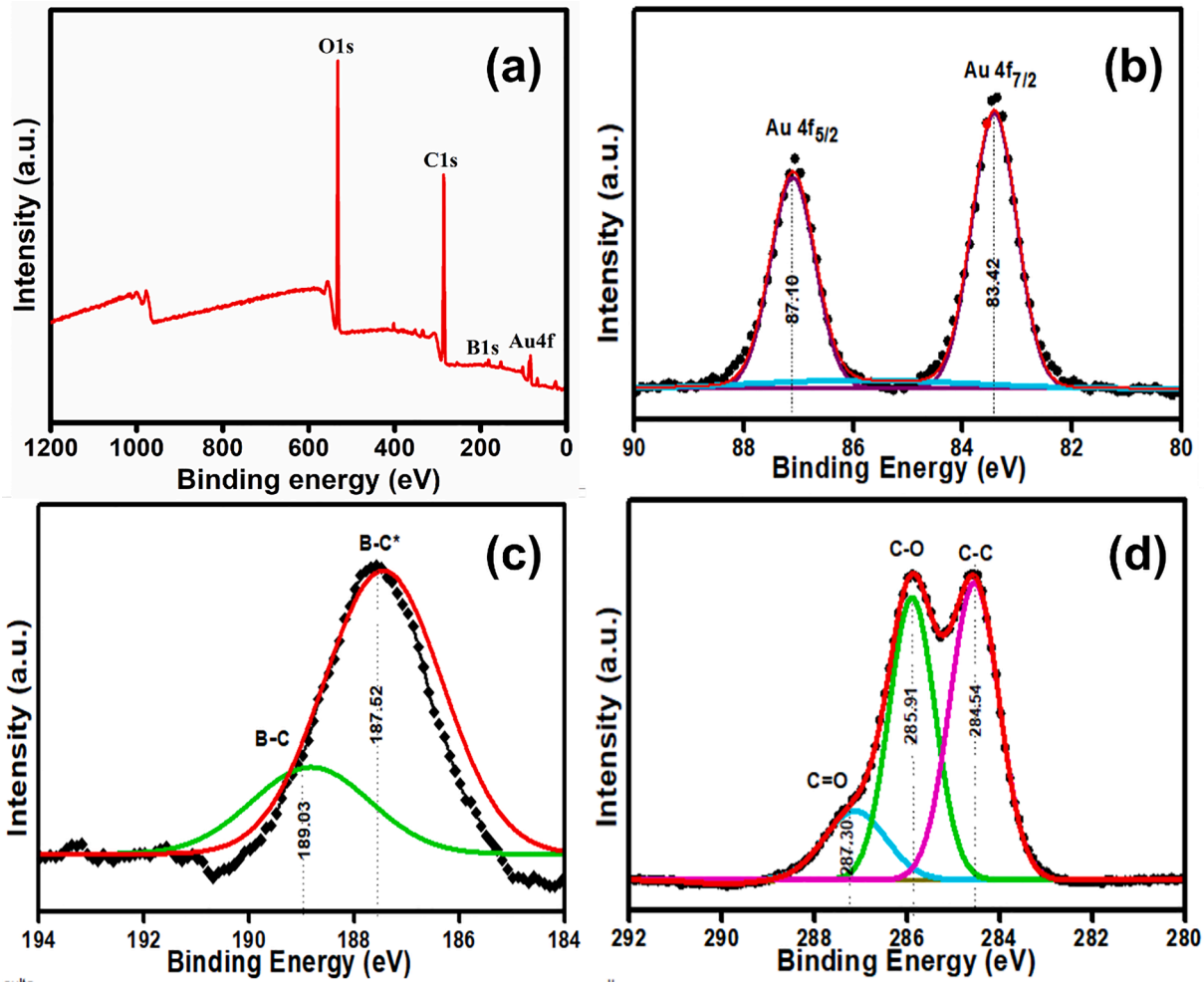

Fig. 5. Au@B-GQDs XPS spectra: (a) Survey spectrum, (b) Au4f, (c) B1s, and (d) C1s high-resolution spectra.

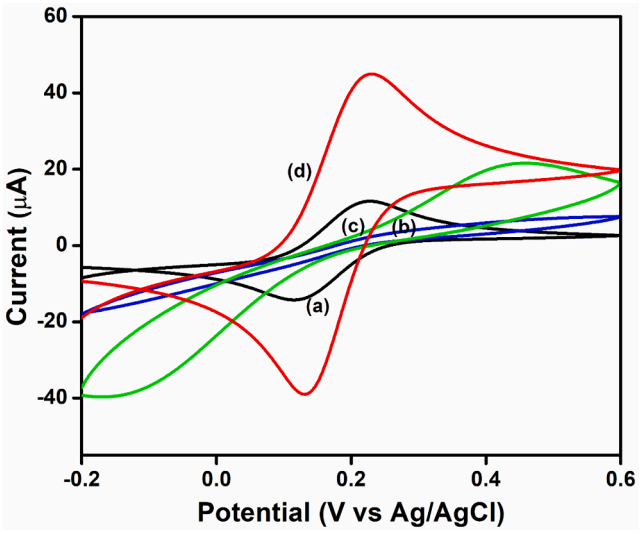

Fig. 6. CVs of (a) Bare/GCE, (b) AuNPs/GCE, (c) B-GQDs/GCE, and (d) Au@B-GQDs/GCE in 5.0 mM $[Fe(CN)_6]^{3-/4-}$ containing 0.1 M KCl. Scan rate: 50mVs^{-1}.

and mass transfer.

Electrochemical investigations were carried out in the presence of GUA and ADE (individually) using various electrodes. Firstly, Fig. 7A shows CVs of the (a) bare/GCE, (b) AuNPs/GCE, (c) B-GQDs/GCE, and (d) Au@B-GQDs/GCE in a 0.1 M phosphate buffer solution with the presence of 25 μM GUA in the potential window ranging from + 0.4 V to + 1.4 V with a scan rate of 50 mV/s. First, in the case of the bare/GC electrode in the chosen potential window, there is no oxidation signal for GUA. This finding suggests that the bare/GCE has almost no electrocatalytic activity for GUA oxidation. For AuNPs/GCE and B-GQDs/GCE, a small broad peak was noted at 0.885 and 0.807 V, respectively. Thus, such nanomaterials show improved electrocatalytic activity toward GUA oxidation upon compared to the bare electrode. However, for Au@B-GQDs modified GC electrode a distinct oxidation peak is observed at 0.811 V with a considerable increment in the current this might be attributable to GUA electrosorption which leads to the generation of adsorbed intermediates. This finding suggested that Au@B-GQDs had high electrocatalytic activity toward GUA oxidation, which may be attributed to a synergistic effect of AuNPs and B-GQDs. The same tests were carried out while accounting for ADE.

Fig. 7B displays CV profiles of the (a) bare/GCE, (b) AuNPs/GCE, (c) B-GQDs/GCE, and (d) Au@B-GQDs/GCE in a 0.1 M phosphate buffer solution with the presence of ADE in the potential window ranging from +0.4 V to +1.4 V with a scan rate of 50 mV/s. As seen before, in the specified potential window, there is no oxidation signal for ADE towards bare/GC electrode. This shows that the bare/GC electrode has relatively low electrocatalytic activity in the oxidation of ADE. Peaks were seen at 1.102 V and 1.05 V for AuNPs/GCE and B-GQDs/GCE, respectively, which are having higher background peak current compared to bare/GC, which results in having a better ability to detect ADE oxidation.

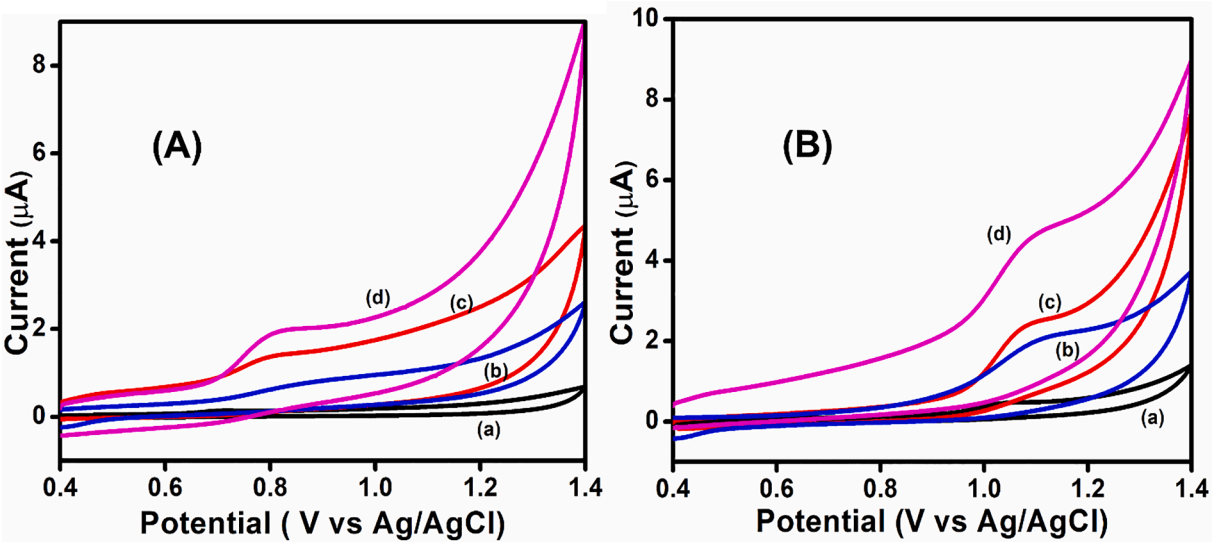

Fig. 7. (A) CVs of (a) bare/GCE, (b) AuNPs/GCE, (c) B-GQDs/GCE, and (d) Au@B-GQDs/GCE in 0.1 M PBS containing 25 μM GUA. (B) CVs of (a) bare/GCE, (b) AuNPs/GCE, (c) B-GQDs/GCE, and (d) Au@B-GQDs/GCE in 0.1 M PBS containing 25 μM ADE. Scan rate: 50mVs^{-1}.

However, for Au@B-GQDs modified GC electrode a distinct oxidation peak was observed at 1.081 V with a considerable rise in background peak current, showing that it has better sensing characteristics than AuNPs and B-GQDs, which again might be attributed to a synergistic effect of AuNPs and B-GQDs.

In the cathodic direction, no peaks were seen, implying that there is just one oxidation wave without reduction, implying that the charge transfer mechanism is irreversible for both analytes. As a result, Scheme 3 depicts the probable process for the oxidation of GUA and ADE [56,57].

The detection of GUA and ADE were also carried out using differential pulse voltammetry-DPV, which is significantly more sensitive and has a greater resolution than CV. Fig. 8A shows differential pulse voltammograms of the (a) bare/GCE, (b) AuNPs/GCE, (c) B-GQDs/GCE, and (d) Au@B-GQDs/GCE in a 0.1 M phosphate buffer solution with the presence of 25 μM GUA in the potential window ranging from +0.4 V to +1.4 V with a scan rate of 10 mV/s. In DPV, peaks are shifted to the left side due to increased sensitivity and lower capacitive currents. At the bare GC electrode, just a slight background current was recorded in 25 μM GUA in pH = 7. In Fig. 8b B-GQDs/GCE shows a relatively broader peak at 0.741 V while AuNPs/GCE (Fig. 8c) shows not a well-defined and much wider peak for the oxidation of GUA. On the other hand, Au@B-GQDs/GCE has a well-defined sharp peak at a lower potential than both B-GQDs and AuNPs at 0.679 V with a much higher current. This lower applied potential suggests that GUA is easy to be oxidized on the Au@B-GQDs/GCE, this indicated that modified Au@B-GQDs/GCE shows good electrocatalytic performance towards guanine oxidation.

Fig. 8B shows the positive-going portions (anodic) of cyclic voltammograms of the fabricated Au@B-GQDs/GC electrode in 0.1 M PBS (pH = 7) containing 25 μM ADE at the scan rate of 10 mV/s. At the bare GC electrode, just a slight background current was recorded in 25 μM ADE in 0.1 M PBS (pH = 7) solution. Au@B-GQDs/GC electrode shows a more significant but wider peak at +1.063 V and +1.035 V respectively upon compared to AuNPs/GCE and B-GQDs/GCE. ADE was oxidized at +1.035 V with a substantial current, implying a negative shift and an increase in current in the presence of Au@B-GQDs/GCE. (Fig. 8d). These results represent that during ADE detection, the Au@B-GQDs can boost the electron transfer rate more than bare and other modified electrodes, which indicates its good catalytic activity towards the ADE sensing. The increase in peak current and a negative shift in the oxidation potential are obvious indications of Au@B-GQDs' electrocatalytic activity in the oxidation of GUA and ADE.

Fig. 9 shows differently modified electrodes at pH 7 with and without 25 μM GUA and 20 μM ADE at the scan rate of 50 mV/s. AuNPs/GCE, B-GQDs/GCE, and Au@B-GQDs/GCE do not exhibit any distinct peaks in the absence of GUA and ADE. However, in the presence of GUA and ADE, AuNPs/GCE and B-GQDs/GCE demonstrate significant oxidation capability at average potentials of +0.8 V for GUA and +1.1 V for ADE.

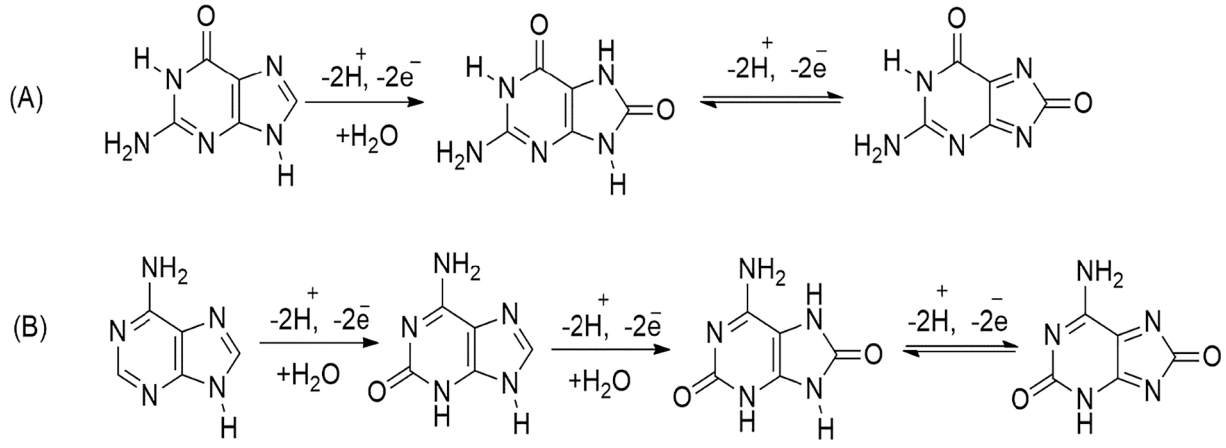

Scheme 3. Oxidation mechanism of guanine (A) and adenine (B).

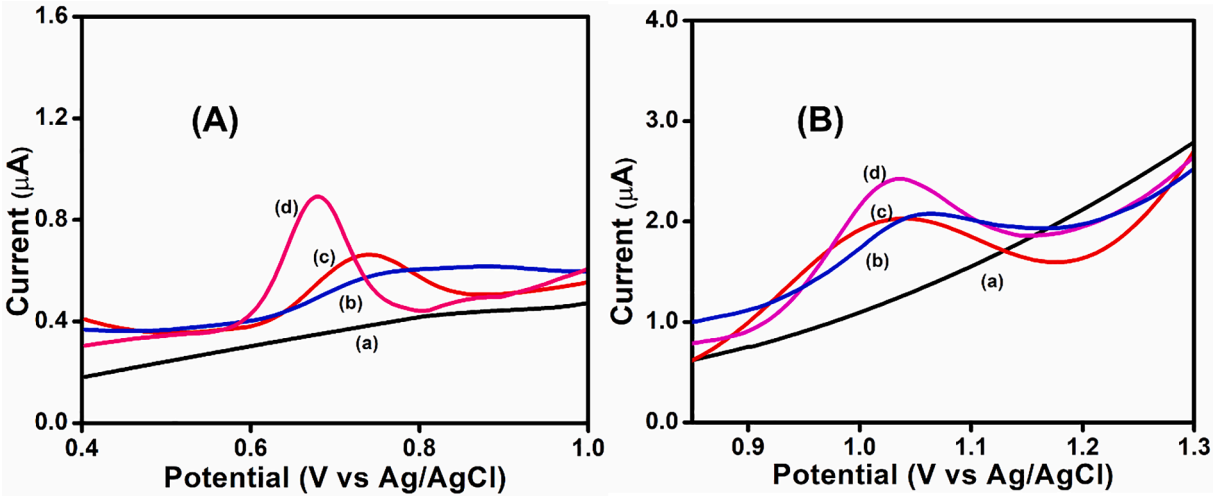

Fig. 8. (A) DPVs of (a) bare/GCE, (b) AuNPs/GCE, (c) B-GQDs/GCE, and (d) Au@B-GQDs/GCE in 0.1 M PBS containing 25 μM GUA. (B) DPVs of (a) bare/GCE, (b) AuNPs/GCE, (c) B-GQDs/GCE, and (d) Au@B-GQDs/GCE in 0.1 M PBS containing 25 μM ADE. Scan rate: 10 mVs^{-1}.

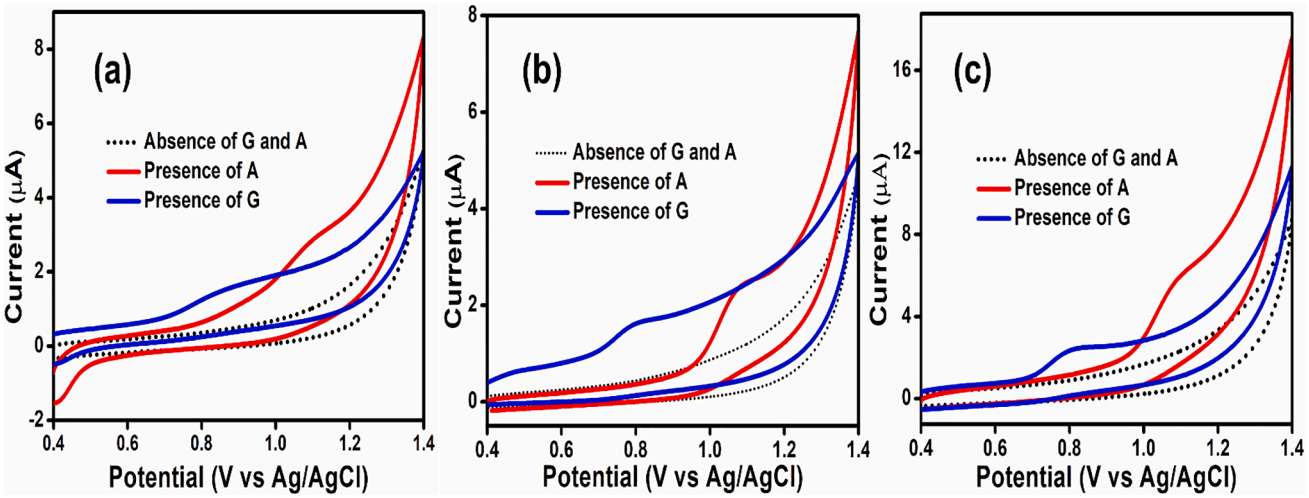

Fig. 9. CVs of AuNPs/GCE (a), B-GQDs/GCE (b), and Au@B-GQDs/GCE (c) in 0.1 M PBS (pH = 7) with and without 25 μM GUA and 20 μM ADE.

However for the fabricated Au@B-GQDs/GC electrode, in the presence of GUA and ADE, a peak was noticed at +0.813 V and +1.075 V. The Au@B-GQDs/GCE nanocomposite, on the other hand, demonstrated a characteristic electrooxidation response to GUA and ADE, indicating that the nanocomposite had strong electrocatalytic activity for these two nucleobases. This may be due to the synergic effect in Au@B-GQDs by the incorporation of gold onto the boron-doped graphene quantum dots.

Further studied the simultaneous determination of GUA and ADE using CV. Fig. 10 shows the CVs of (a) bare/GCE, (b) AuNPs/GCE, (c) B-GQDs/GCE, and (d) Au@B-GQDs/GCE in a 0.1 M phosphate buffer solution with the presence of both GUA (25 μM) and ADE (20 μM) in the potential window ranging from +0.4 V to +1.4 V at a scan rate of 50 mV/s. In Fig. 10, the bare/GC electrode did not show any peaks implying it has negligible electrocatalytic activity towards the GUA and ADE oxidation. In the case of AuNPs/GCE, two broad peaks of low current intensity were observed at +0.781 and +1.079 V for GUA and ADE respectively (Fig. 10b). Likewise, B-GQDs/GCE (Fig. 10c) also shows two peaks of relatively low current intensity for GUA and ADE, respectively, at +0.708 and +0.9845 V. The current response of Au@B-GQDs/GC electrode to GUA and ADE is quite strong and sharp, with two peaks at +0.743 and +1.052 V, respectively. These findings reveal that modified Au@B-GQDs are capable of effectively detecting GUA and ADE simultaneously in a mixture.

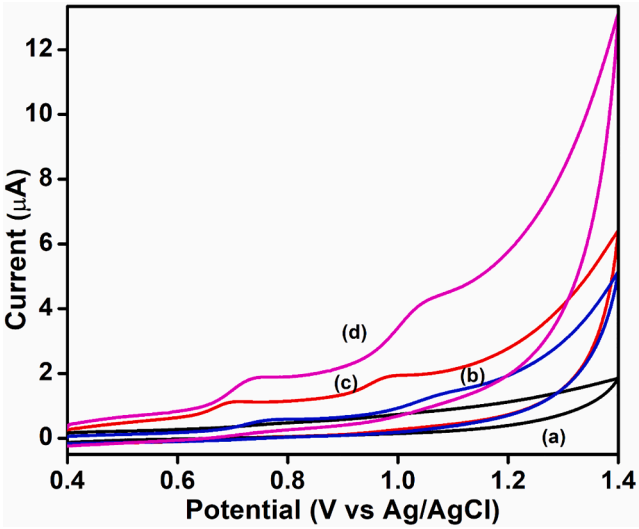

Fig. 10. CVs of (a) bare/GCE, (b) AuNPs/GCE, (c) B-GQDs/GCE, and (d) Au@B-GQDs/GCE in 0.1 M PBS containing 25 μM GUA and 20 μM ADE. Scan rate: 50 mVs^{-1}.

Using CV, the effect of scan rate at Au@B-GQDs modified GC electrode was examined in 0.1 M PBS solution (pH = 7.0) containing 25 μM GUA and 20 μM ADE (Fig. 11) shows only anodic peaks of GUA and ADE which illustrate that purine base oxidation on the modified electrode is irreversible. The anodic peak currents of GUA and ADE are seen to increase linearly upon increasing the scan rate from 20 to 200 mV/s range, which suggests that the electrocatalytic oxidation of GUA and ADE at the Au@B-GQDs electrode is a surface-controlled process.

The determination of GUA and ADE simultaneously with an increment in the concentration at Au@B-GQDs/GC electrode was cross-examined by using DPV in Fig. 12. The concentrations of GUA and ADE were changed from 10 to 140 μM in 0.1 M PBS solution at a scan rate of 10 mV/s. The anodic peak responses for the binary mixtures including GUA and ADE are well separated, with a potential difference of 330 mV according to DPV experiments. The response current related to the analyte oxidation increases as the binary mixture concentration rises. The resulting current is proportional to the analyte concentration in the reaction vessel. A linear rise in current intensity as a function of increasing concentration of GUA and ADE can be observed.

As purine bases (GUA and ADE) coexist in DNA, simultaneous identification of both is critical from a diagnostic standpoint. The coexistent solution with different concentrations of GUA and ADE was detected by DPV by attempting to measure the sensor's performance in terms of individual determination of each using an Au@B-GQDs modified GC electrode. The concentration of one analyte was altered in this investigation, while the concentration of another analyte remained constant (Fig. 13). The intensity of the oxidation peak current for the tested analyte increased, meanwhile, the current intensity of the others remained steady, indicating that there was no interference impact between them. These findings show that these purine bases can be identified in a combination at the concentration range examined. In Fig. 13A, the concentration of GUA was changed from 0.5 to 20 μM while the concentration of ADE was kept constant at 5 μM in 0.1 M PBS solution with a DPV (scan rate of 10 mV/s). It was observed that as the concentration of GUA was raised, the response current to GUA grew as well, whereas the response current to ADE remained nearly constant. Two distinct oxidation peaks are detected corresponding to the oxidation of GUA and ADE. The linear range of 0.5–20 μM towards GUA sensing with a low limit of detection at 1.71 μM with the sensitivity of 0.082 μAμM^{-1}. In Fig. 13B, the concentration of ADE was changed from 0.1 to 20 μM, and GUA was kept constant at 5 μM in 0.1 M PBS solution with a DPV (scan rate of 10 mV/s). The response current to ADE increased as the concentration of ADE increased, but the response current to GUA remained practically constant. The oxidation of GUA and ADE is represented by two well-defined oxidation peaks. The peak-to-peak spacing is 300 mV, indicating that both ADE and GUA may be well detected together. The linear range of 0.1–20 μM towards ADE sensing with a low detection limit of 1.84 μM with the sensitivity of 0.156 μAμM^{-1}. A good linear response, limit of detection, and sensitivity to either GUA or ADE concentrations are obtained. Thus, the proposed Au@B-GQDs/GC electrode may be employed for the sensitive and selective detection of GUA and ADE. Table 1 summarizes a comparison of detection limit and linear range utilizing Au@B-GQDs/GC electrode to several modified electrodes in the literature. The proposed Au@B-GQDs/GC electrode showed enhanced dynamic range and LOD for GUA and ADE which are comparable with the previously reported electrodes. This comparison revealed the ability of the Au@B-GQDs/GCE sensor to accomplish the simultaneous detection of GUA and ADE.

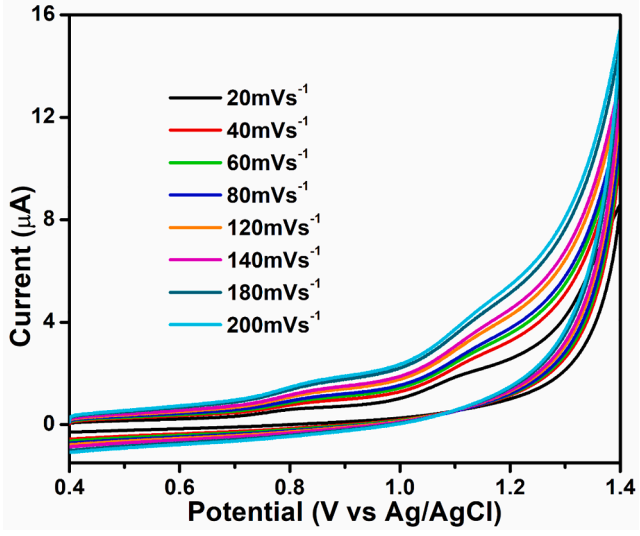

Fig. 11. CV of Au@B-GQDs/GCE in 0.1 M PBS containing 25 μM GUA and 20 μM ADE with varying scan rates from 20 to 200mVs^{-1}.

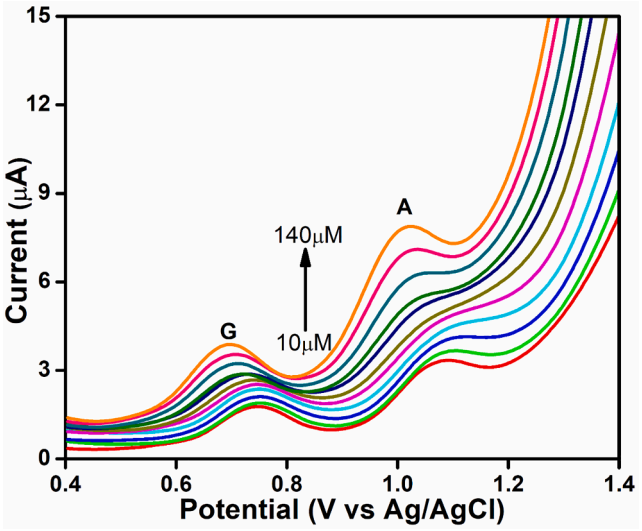

Fig. 12. DPVs of Au@B-GQDs in 0.1 M PBS containing 10–140 μM of GUA and ADE each. Scan rate: 10mVs^{-1}.

Selectivity is one of the desirable basic requirements for sensor applications. The selectivity of the Au@B-GQDs modified electrode for sensitive detection of GUA and ADE, as well as a number of important metal ions and biological substances that could interfere with the results, were investigated. The effects of these interfering species were investigated by measuring 25 μM GUA and ADE in the presence of various concentrations of the interferents in the PBS (pH = 7) electrolyte (Fig. S3). It can be seen that ascorbic acid, glucose, urea, uric acid, and inorganic ions such as Ca^{2+}, Fe^{3+}, Na^{+}, K^{+} had a negligible effect on the determination of GUA and ADE (signal change <10%). As a result of the anti-interference properties, the newly designed Au@B-GQDs/GC electrode appears to be a potential technique used to detect GUA and ADE in biological matrixes.

Fig. S4 shows the long-lasting stability of the prepared Au@B-GQDs/GC electrode studied over five weeks during which the electrode was kept at a temperature of 4 °C. The tests were carried out with a solution of 25 μM GUA and 20 μM ADE dissolved in PBS (0.1 M pH 7.0). After 5 weeks, the modified electrode retained 83% and 88% of their initial current response of GUA and ADE, respectively, proving that the electrode's detection capability is satisfactory for a sufficient period. The chemical stability of AuNPs and B-GQDs in the redesigned Au@B-GQDs/GC electrode might explain these results. It signifies that the prepared electrode is quite stable over a sufficient period. The reproducibility of the proposed sensor is demonstrated in Fig. S5 by serial detection of 25 μM GUA and 20 μM ADE in PBS solution (0.1 M pH 7.0). The relative standard deviations (RSD) were estimated to be 1.9 % for GUA and 5.0 % for ADE using five independently designed electrodes, exhibiting high reproducibility. The repeatability of the constructed electrodes was

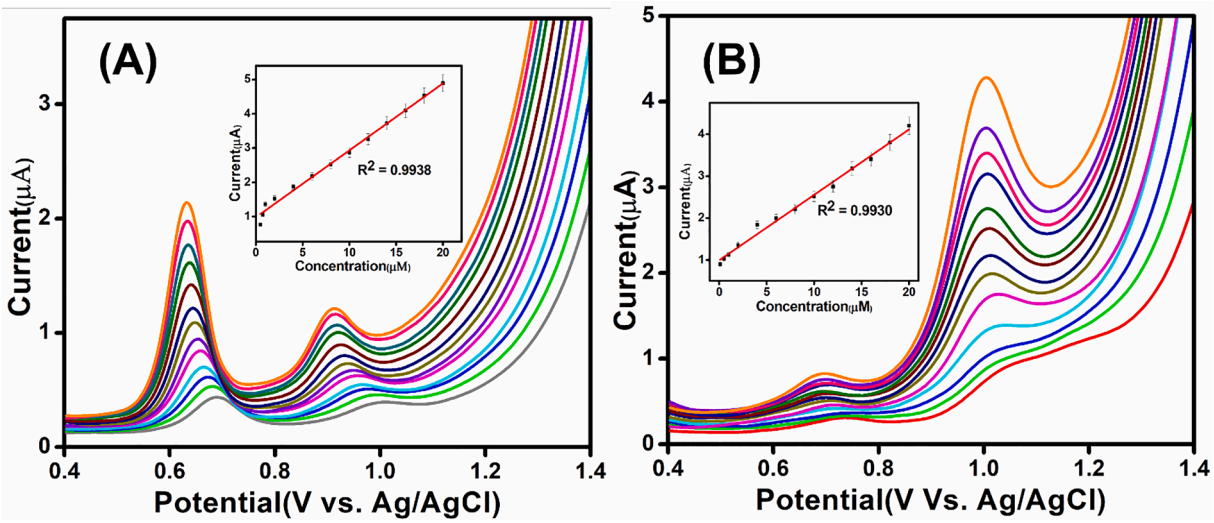

Fig. 13. (A) DPV of Au@B-GQDs/GCE in 0.1 M PBS containing 0.5–20 μM GUA and 5 μM ADE. Scan rate:10 mV/s. Inset: Plot of peak current as a function of the concentration of GUA. (B) DPV of Au@B-GQDs/GCE in 0.1 M PBS containing 5 μM GUA and 0.1–20 μM ADE. Scan rate:10 mV/s. Inset: Plot of peak current as a function of the concentration of ADE.

Table 1
Comparison of detection limit using Au@B-GQDs/GC electrode to various modified electrode previously reported in the literature.

Electrodes	Dynamic Range (μM)		Limit of Detection (μM)		References
	GUA	ADE	GUA	ADE	
Au/HG electrode	6–500	0.6–40	2.5	0.42	[40]
MWCNT- Fe_3O_4@PDA-Ag/ GCE	8–130	10–120	1.47	5.66	[58]
Au-rGO/MWNCT/graphite	3–170	3–190	3.3	3.7	[59]
PANI/MnO_2/GCE	10–100	10–100	4.8	2.9	[46]
Au paste electrode	3–23	3.9–69.3	1.3	0.74	[60]
Au@B-GQDs/ GCE	0.5–20	0.1–20	1.71	1.84	This Work

assessed by repeating the voltammetric responses five times with the same electrode, as shown in Fig. S6, and its effects on the peak currents of 25 μM each of GUA and 20 μM ADE in pH 7.0. With 5 consecutive measurements, the RSD was found to be 4.6 % for GUA and 4.5 % for ADE.

3.3. Detection of GUA and ADE in real sample

The applicability of the proposed sensor Au@B-GQDs/GC electrode in biological samples for the determination of GUA and ADE was evaluated in a thermally denatured calf thymus DNA sample. The material was pretreated as outlined in the experimental section prior to analysis. A spike recovery analysis was performed on the sample matrix at two different concentrations and the obtained results are presented in Table 2. The standard addition method was used to test the recovery. This was established by adding a known concentration of guanine and adenine to the HCl digested calf thymus DNA sample. The high recovery rates of 99 to 102 % for GUA and ADE in calf thymus DNA demonstrated the Au@B-GQDs/GC electrode electrochemical sensor's accuracy in determining GUA and ADE bases in actual samples in the presence of interferents.

Table 2
Determination of GUA and ADE using standard addition method in real sample (n = 3).

Sample	Analyte	Detected (μA)	Added (μM)	Found (μA)	Recovery rate %
1	**Guanine**	1.3 ± 1.1	10	11.1 ± 1.2	99.0
	Adenine	4.8 ± 1.4	20	25 ± 1.7	101.0
2	**Guanine**	1.31 ± 1.2	30	31.1 ± 1.9	99.3
	Adenine	4.7 ± 1.3	10	14.9 ± 1.7	102.0

4. Conclusions

In this work, it has been manifested that the synthesis of Au@B-GQDs nanocomposite can be successfully prepared by sonochemical reduction. The fabricated Au@B-GQDs/GC electrode exhibit very attractive electrocatalytic activity towards GUA and ADE oxidation in neutral media and the synergetic effects between AuNPs and B-GQDs is helpful to improve the electrocatalytic activity in ADE and GUA oxidation. The experimental results show Au@B-GQDs nanoparticles have much higher electrocatalytic activity than AuNPs and B-GQDs. Furthermore with common interfering biomolecules (glucose, uric acid, urea, and ascorbic acid), the produced electrochemical sensor exhibits amazing stability, outstanding reproducibility, and good repeatability. In real sample analysis, the newly designed Au@B-GQDs/GC electrode demonstrates its operational flexibility and good recovery yield in the GUA and ADE determination. The existence of edge defects in quantum dots aids in the adsorption of additional metal ions, and doping aids in the insertion process, which results outstanding electrooxidation responses towards GUA and ADE. As a result of this research, a novel method for creating zero-dimensional carbon nanostructures has been developed, as well as a new avenue for developing new types of materials for electrochemical sensing.

CRediT authorship contribution statement

Reshma Kaimal: Investigation, Data curation, Validation, Writing – original draft. **Patel Nishant Mansukhlal:** Formal analysis, Data curation. **Belqasem Aljafari:** Visualization, Writing – review & editing. **Sambandam Anandan:** Conceptualization, Supervision, Methodology, Writing – review & editing, Resources. **Muthupandian Ashokkumar:** Resources, Writing – review & editing.

Declaration of Competing Interest

The authors declare that they have no known competing financial interests or personal relationships that could have appeared to influence the work reported in this paper.

Acknowledgements

Ms. Reshma expresses gratitude to the MHRD for the Ph.D. fellowship. Also authors Anandan and Ashokkumar thank India-Australia collaboration project under SPARC (SPARC/2018-2019/P236/SL) scheme.

Appendix A. Supplementary data

Supplementary data to this article can be found online at https://doi.org/10.1016/j.ultsonch.2022.105921.

References

[1] Q. Shen, X. Wang, Simultaneous determination of adenine, guanine and thymine based on β-cyclodextrin/MWNTs modified electrode, J. Electroanal. Chem. 632 (1-2) (2009) 149–153, https://doi.org/10.1016/j.jelechem.2009.04.009.
[2] A.R. Lehmann, DNA polymerases and repair synthesis in NER in human cells, DNA Repair (Amst). 10 (7) (2011) 730–733, https://doi.org/10.1016/j.dnarep.2011.04.023.
[3] J. Wang, Electrochemical nucleic acid biosensors, Anal. Chim. Acta. 469 (1) (2002) 63–71, https://doi.org/10.1016/S0003-2670(01)01399-X.
[4] R. Thangaraj, A. Senthil Kumar, Simultaneous detection of guanine and adenine in DNA and meat samples using graphitized mesoporous carbon modified electrode, J. Solid State Electrochem. 17 (3) (2013) 583–590, https://doi.org/10.1007/s10008-012-1895-0.
[5] P. Cekan, S.T. Sigurdsson, Identification of single-base mismatches in duplex DNA by EPR spectroscopy, J. Am. Chem. Soc. 131 (50) (2009) 18054–18056, https://doi.org/10.1021/ja905623k.
[6] A. Pietrzyk, S. Suriyanarayanan, W. Kutner, R. Chitta, M.E. Zandler, F. D'Souza, Molecularly imprinted polymer (MIP) based piezoelectric microgravimetry chemosensor for selective determination of adenine, Biosens. Bioelectron. 25 (11) (2010) 2522–2529, https://doi.org/10.1016/j.bios.2010.04.015.
[7] F. Jelen, A.B. Olejniczak, A. Kourilova, Z.J. Lesnikowski, E. Palecek, Electrochemical DNA detection based on the polyhedral boron cluster label, Anal. Chem. 81 (2) (2009) 840–844, https://doi.org/10.1021/ac801235b.
[8] A. Abbaspour, A. Ghaffarinejad, Preparation of a sol-gel-derived carbon nanotube ceramic electrode by microwave irradiation and its application for the determination of adenine and guanine, Electrochim. Acta. 55 (3) (2010) 1090–1096, https://doi.org/10.1016/j.electacta.2009.09.065.
[9] T. Furukawa, M.J. Curtis, C.M. Tominey, Y.H. Duong, B.W.L. Wilcox, D. Aggoune, J.B. Hays, A.B. Britt, A shared DNA-damage-response pathway for induction of stem-cell death by UVB and by gamma irradiation, DNA Repair (Amst). 9 (9) (2010) 940–948, https://doi.org/10.1016/j.dnarep.2010.06.006.
[10] J.B. Hays, New analytical methods for genetic dissection of biological responses to DNA lesions, DNA Repair (Amst). 10 (5) (2011) 526–535, https://doi.org/10.1016/j.dnarep.2011.02.006.
[11] M. Su, W. Wei, S. Liu, Analytical applications of the electrochemiluminescence of tris(2,2'-bipyridyl)ruthenium(II) coupled to capillary/microchip electrophoresis: A review, Anal. Chim. Acta. 704 (1-2) (2011) 16–32, https://doi.org/10.1016/j.aca.2011.07.016.
[12] M.H. Ghanim, M.Z. Abdullah, Integrating amperometric detection with electrophoresis microchip devices for biochemical assays: recent developments, Talanta 85 (1) (2011) 28–34, https://doi.org/10.1016/j.talanta.2011.04.069.
[13] H.-J. Zeng, R. Yang, Q.-W. Wang, J.-J. Li, L.-b. Qu, Determination of melamine by flow injection analysis based on chemiluminescence system, Food Chem. 127 (2) (2011) 842–846, https://doi.org/10.1016/j.foodchem.2011.01.021.
[14] H. Qiu, Y. Xi, F. Lu, L. Fan, C. Luo, Determination of L-phenylalanine on-line based on molecularly imprinted polymeric microspheres and flow injection chemiluminescence, Spectrochim. Acta - Part A Mol. Biomol. Spectrosc. 86 (2012) 456–460, https://doi.org/10.1016/j.saa.2011.10.068.
[15] H. Yu, Y. Tao, D. Chen, Y. Wang, L. Huang, D. Peng, M. Dai, Z. Liu, X.u. Wang, Z. Yuan, Development of a high performance liquid chromatography method and a liquid chromatography-tandem mass spectrometry method with the pressurized liquid extraction for the quantification and confirmation of sulfonamides in the foods of animal origin, J. Chromatogr. B Anal. Technol. Biomed Life Sci. 879 (25) (2011) 2653–2662, https://doi.org/10.1016/j.jchromb.2011.07.032.
[16] H.C. Chen, Y.S. Chang, S.J. Chen, P.L. Chang, Determination of the heterogeneity of DNA methylation by combined bisulfite restriction analysis and capillary electrophoresis with laser-induced fluorescence, J. Chromatogr. A. 1230 (2012) 123–129, https://doi.org/10.1016/j.chroma.2012.01.049.
[17] X. Zhang, Z. Zhang, Sweeping under controlled electroosmotic flow and micellar electrokinetic chromatography for on-line concentration and determination of trace phlorizin and quercitrin in urine samples, J. Pharm. Biomed. Anal. 56 (2) (2011) 330–335, https://doi.org/10.1016/j.jpba.2011.05.016.
[18] W. Sun, Y. Li, Y. Duan, K. Jiao, Direct electrochemistry of guanosine on multi-walled carbon nanotubes modified carbon ionic liquid electrode, Electrochim. Acta. 54 (16) (2009) 4105–4110, https://doi.org/10.1016/j.electacta.2009.02.041.
[19] E. Paleček, M. Bartošík, Electrochemistry of nucleic acids, Chem. Rev. 112 (6) (2012) 3427–3481, https://doi.org/10.1021/cr200303p.
[20] M. Bacon, S.J. Bradley, T. Nann, Graphene quantum dots, Part. Part. Syst. Charact. 31 (4) (2014) 415–428, https://doi.org/10.1002/ppsc.201300252.
[21] J. Shen, Y. Zhu, X. Yang, J. Zong, J. Zhang, C. Li, One-pot hydrothermal synthesis of graphene quantum dots surface-passivated by polyethylene glycol and their photoelectric conversion under near-infrared light, New J. Chem. 36 (1) (2012) 97–101.
[22] Y. Dong, C. Chen, X. Zheng, L. Gao, Z. Cui, H. Yang, C. Guo, Y. Chi, C.M. Li, One-step and high yield simultaneous preparation of single- and multi-layer graphene quantum dots from CX-72 carbon black, J. Mater. Chem. 22 (2012) 8764–8766, https://doi.org/10.1039/c2jm30658a.
[23] V. Gupta, N. Chaudhary, R. Srivastava, G.D. Sharma, R. Bhardwaj, S. Chand, Luminscent graphene quantum dots for organic photovoltaic devices, J. Am. Chem. Soc. 133 (26) (2011) 9960–9963, https://doi.org/10.1021/ja2036749.
[24] L.S. Panchakarla, K.S. Subrahmanyam, S.K. Saha, A. Govindaraj, H. R. Krishnamurthy, U.V. Waghmare, C.N.R. Rao, Synthesis, structure, and properties of boron- and nitrogen-doped graphene, Adv. Mater. 21 (2009) 4726–4730, https://doi.org/10.1002/adma.200901285.
[25] Z. Guan, W. Wang, J. Huang, X. Wu, Q. Li, J. Yang, Tunable electronic and magnetic properties of graphene flake-doped boron nitride nanotubes, J. Phys. Chem. C. 118 (49) (2014) 28616–28624, https://doi.org/10.1021/jp5089349.
[26] R. Lv, G. Chen, Q. Li, A. McCreary, A. Botello-Méndez, S.V. Morozov, L. Liang, X. Declerck, N. Perea-López, D.A. Cullen, S. Feng, A.L. Elías, R. Cruz-Silva, K. Fujisawa, M. Endo, F. Kang, J.-C. Charlier, V. Meunier, M. Pan, A. R. Harutyunyan, K.S. Novoselov, M. Terrones, Ultrasensitive gas detection of large-area boron-doped graphene, Proc. Natl. Acad. Sci. U. S. A. 112 (47) (2015) 14527–14532, https://doi.org/10.1073/pnas.1505993112.
[27] B. Biel, X. Blase, F. Triozon, S. Roche, Anomalous doping effects on charge transport in graphene nanoribbons, Phys. Rev. Lett. 102 (2009) 1–4, https://doi.org/10.1103/PhysRevLett.102.096803.
[28] H. Terrones, R. Lv, M. Terrones, M.S. Dresselhaus, The role of defects and doping in 2D graphene sheets and 1D nanoribbons, Reports Prog. Phys. 75 (6) (2012) 062501, https://doi.org/10.1088/0034-4885/75/6/062501.
[29] Z.-S. Wu, W. Ren, L.i. Xu, F. Li, H.-M. Cheng, Doped graphene sheets as anode materials with superhigh rate and large capacity for lithium ion batteries, ACS Nano 5 (7) (2011) 5463–5471, https://doi.org/10.1021/nn2006249.
[30] Y. Huang, C. Zhu, H. Pan, D. Xu, T. Lu, L. Mao, X. Meng, Z. Chen, D. Zhang, S. Zhu, Fabrication of AgBr/boron-doped reduced graphene oxide aerogels for photocatalytic removal of Cr(VI) in water, RSC Adv. 7 (2017) 36000–36006, https://doi.org/10.1039/c7ra05770a.
[31] Z. Ding, M. Sun, W. Liu, W. Sun, X. Meng, Y. Zheng, Ultrasonically synthesized N-TiO2/Ti3C2 composites: enhancing sonophotocatalytic activity for pollutant degradation and nitrogen fixation, Sep. Purif. Technol. 276 (2021) 119287, https://doi.org/10.1016/j.seppur.2021.119287.
[32] W. Liu, M. Sun, Z. Ding, Q.i. Zeng, Y. Zheng, W. Sun, X. Meng, Ball milling synthesis of porous g-C3N4 ultrathin nanosheets functionalized with alkynyl groups for strengthened photocatalytic activity, Sep. Purif. Technol. 282 (2022) 120097, https://doi.org/10.1016/j.seppur.2021.120097.
[33] B. Gao, M. Sun, W. Ding, Z. Ding, W. Liu, Decoration of γ-graphyne on TiO2 nanotube arrays: Improved photoelectrochemical and photoelectrocatalytic properties, Appl. Catal. B Environ. 281 (2021) 119492, https://doi.org/10.1016/j.apcatb.2020.119492.
[34] X. Lin, M. Sun, B. Gao, W. Ding, Z. Zhang, S. Anandan, A. Umar, Hydrothermally regulating phase composition of TiO2 nanocrystals toward high photocatalytic activity, J. Alloys Compd. 850 (2021) 156653, https://doi.org/10.1016/j.jallcom.2020.156653.
[35] W. Liu, M. Sun, Z. Ding, B. Gao, W. Ding, Ti3C2 MXene embellished g-C3N4 nanosheets for improving photocatalytic redox capacity, J. Alloys Compd. 877 (2021) 160223, https://doi.org/10.1016/j.jallcom.2021.160223.
[36] S. Guo, E. Wang, Synthesis and electrochemical applications of gold nanoparticles, Anal. Chim. Acta. 598 (2) (2007) 181–192, https://doi.org/10.1016/j.aca.2007.07.054.
[37] G. Li, T. Li, Y. Deng, Y. Cheng, F. Shi, W. Sun, Z. Sun, Electrodeposited nanogold decorated graphene modified carbon ionic liquid electrode for the electrochemical myoglobin biosensor, J. Solid State Electrochem. 17 (8) (2013) 2333–2340, https://doi.org/10.1007/s10008-013-2098-z.
[38] J.R. Siqueira, R.C. Gabriel, L.H.S. Gasparotto, Layer-by-layer assembly of poly (vinylpyrrolidone)-embedded gold nanoparticles with carbon nanotubes for glycerol electro-oxidation, J. Mater. Sci. 51 (18) (2016) 8323–8330, https://doi.org/10.1007/s10853-016-0061-y.
[39] V. Vinoth, T.M.D'. Rozario, J.J. Wu, S. Anandan, M. Ashokkumar, Graphene quantum dots anchored gold nanorods for electrochemical detection of glutathione, ChemistrySelect. 2 (17) (2017) 4744–4752, https://doi.org/10.1002/slct.201700845.
[40] S. Gao, H. Li, M. Li, C. Li, L. Qian, B. Yang, A gold-nanoparticle/horizontal-graphene electrode for the simultaneous detection of ascorbic acid, dopamine, uric acid, guanine, and adenine, J. Solid State Electrochem. 22 (10) (2018) 3245–3254, https://doi.org/10.1007/s10008-018-4019-7.

[41] M.R. Langille, M.L. Personick, J. Zhang, C.A. Mirkin, Defining rules for the shape evolution of gold nanoparticles, J. Am. Chem. Soc. 134 (35) (2012) 14542–14554, https://doi.org/10.1021/ja305245g.
[42] T.H. Ha, H.-J. Koo, B.H. Chung, Shape-controlled syntheses of gold nanoprisms and nanorods influenced by specific adsorption of halide ions, J. Phys. Chem. C. 111 (3) (2007) 1123–1130, https://doi.org/10.1021/jp066454l10.1021/jp066454l.s001.
[43] M. Sun, G. Ran, Q. Fu, W. Xu, The effect of iodide on the synthesis of gold nanoprisms, J. Exp. Nanosci. 10 (17) (2015) 1309–1318, https://doi.org/10.1080/17458080.2014.1003340.
[44] L. Chen, F. Ji, Y. Xu, L. He, Y. Mi, F. Bao, B. Sun, X. Zhang, Q. Zhang, High-yield seedless synthesis of triangular gold nanoplates through oxidative etching, Nano Lett. 14 (12) (2014) 7201–7206, https://doi.org/10.1021/nl504126u.
[45] T. Van Tam, S.G. Kang, K.F. Babu, E.-S. Oh, S.G. Lee, W.M. Choi, Synthesis of B-doped graphene quantum dots as a metal-free electrocatalyst for the oxygen reduction reaction, J. Mater. Chem. A. 5 (21) (2017) 10537–10543, https://doi.org/10.1039/C7TA01485F.
[46] M.U. Anu Prathap, R. Srivastava, B. Satpati, Simultaneous detection of guanine, adenine, thymine, and cytosine at polyaniline/MnO2 modified electrode, Electrochim. Acta. 114 (2013) 285–295, https://doi.org/10.1016/j.electacta.2013.10.064.
[47] G. Zhang, J.B. Jasinski, J.L. Howell, D. Patel, D.P. Stephens, A.M. Gobin, Tunability and stability of gold nanoparticles obtained from chloroauric acid and sodium thiosulfate reaction, Nanoscale Res. Lett. 7 (2012) 337, https://doi.org/10.1186/1556-276X-7-337.
[48] X. Hai, Q.-X. Mao, W.-J. Wang, X.-F. Wang, X.-W. Chen, J.-H. Wang, An acid-free microwave approach to prepare highly luminescent boron-doped graphene quantum dots for cell imaging, J. Mater. Chem. B. 3 (47) (2015) 9109–9114, https://doi.org/10.1039/C5TB01954K.
[49] F.A. Permatasari, A.H. Aimon, F. Iskandar, T. Ogi, K. Okuyama, Role of C-N configurations in the photoluminescence of graphene quantum dots synthesized by a hydrothermal route, Sci. Rep. 6 (2016) 21042, https://doi.org/10.1038/srep21042.
[50] L.i. Zhang, Z.-Y. Zhang, R.-P. Liang, Y.-H. Li, J.-D. Qiu, Boron-doped graphene quantum dots for selective glucose sensing based on the “abnormal” aggregation-induced photoluminescence enhancement, Anal. Chem. 86 (9) (2014) 4423–4430, https://doi.org/10.1021/ac500289c.
[51] K.N. Kudin, B. Ozbas, H.C. Schniepp, R.K. Prud’homme, I.A. Aksay, R. Car, Raman spectra of graphite oxide and functionalized graphene sheets, Nano Lett. 8 (1) (2008) 36–41, https://doi.org/10.1021/nl071822y.
[52] A.P. Vijaya Kumar Saroja, M.S. Garapati, R. ShyiamalaDevi, M. Kamaraj, S. Ramaprabhu, Facile synthesis of heteroatom doped and undoped graphene quantum dots as active materials for reversible lithium and sodium ions storage, Appl. Surf. Sci. 504 (2020) 144430, https://doi.org/10.1016/j.apsusc.2019.144430.
[53] F.-X. Ma, J. Wang, F.-B. Wang, X.-H. Xia, The room temperature electrochemical synthesis of N-doped graphene and its electrocatalytic activity for oxygen reduction, Chem. Commun. 51 (7) (2015) 1198–1201.
[54] Q. Ding, Z. Kang, X. He, M. Wang, M. Lin, H. Lin, D.-P. Yang, Eggshell membrane-templated gold nanoparticles as a flexible SERS substrate for detection of thiabendazole, Microchim. Acta. 186 (2019) 453, https://doi.org/10.1007/s00604-019-3543-1e.
[55] P.M. Vijaya, M.P. Kumar, C. Takahashi, S. Kundu, T.N. Narayanan, D. K. Pattanayak, Boron-doped graphene quantum dots: An efficient photoanode for a dye sensitized solar cell, New J. Chem. 43 (36) (2019) 14313–14319.
[56] A. Abbaspour, A. Noori, Electrochemical studies on the oxidation of guanine and adenine at cyclodextrin modified electrodes, Analyst. 133 (2008) 1664–1672, https://doi.org/10.1039/b806920d.
[57] R. Manikandan, P.N. Deepa, S.S. Narayanan, Simultaneous electrochemical determination of adenine and guanine using poly 2-naphthol orange film-modified electrode, Ionics 26 (3) (2020) 1475–1482, https://doi.org/10.1007/s11581-019-03279-9.
[58] A. Yari, S. Derki, New MWCNT-Fe3O4@PDA-Ag nanocomposite as a novel sensing element of an electrochemical sensor for determination of guanine and adenine contents of DNA, Sensors Actuators, B Chem. 227 (2016) 456–466, https://doi.org/10.1016/j.snb.2015.12.088.
[59] K.L. Ng, S.M. Khor, Graphite-based nanocomposite electrochemical sensor for multiplex detection of adenine, guanine, thymine, and cytosine: a biomedical prospect for studying DNA damage, Anal. Chem. 89 (18) (2017) 10004–10012, https://doi.org/10.1021/acs.analchem.7b02432.
[60] J. Jankowska-Śliwińska, M. Dawgul, J. Kruk, D.G. Pijanowska, Comparison of electrochemical determination of purines and pyrimidines by means of carbon, graphite and gold paste electrodes, Int. J. Electrochem. Sci. 12 (2017) 2329–2343, https://doi.org/10.20964/2017.03.16.